Deformation mechanisms of CoCrFeMnNi high-entropy alloy under low-cycle-fatigue loading

Kaiju Lu[1*], Ankur Chauhan[1**], Aditya Srinivasan Tirunilai[2], Jens Freudenberger[3,4], Alexander Kauffmann[2], Martin Heilmaier[2], and Jarir Aktaa[1]

email: *kaiju.lu@kit.edu; **ankurskchauhan@gmail.com

[1]Institute for Applied Materials (IAM-WBM), Karlsruhe Institute of Technology (KIT), Hermann-von-Helmholtz-Platz 1, 76344 Eggenstein Leopoldshafen, Germany

[2]Institute for Applied Materials (IAM-WK), Karlsruhe Institute of Technology (KIT), Engelbert-Arnold-Strasse 4, 76131 Karlsruhe, Germany

[3]Leibniz Institute for Solid State and Materials Research Dresden (IFW Dresden), Helmholtzstr. 20, D-01069 Dresden, Germany

[4]Institute of Materials Science, Technische Universität Bergakademie Freiberg, Gustav-Zeuner-Str. 5, 09599 Freiberg, Germany

Abstract

Plastic deformation during low-cycle fatigue (LCF) in equiatomic face-centered cubic (FCC) CoCrFeMnNi high-entropy alloys (HEAs) is accumulated by dislocation substructure formation, which leads to crack initiation. Whilst these substructures have been reported before, little has been done to clarify their formation mechanisms and the effects of strain amplitude, cycle number and grain orientation. In this study, cyclic deformation behavior and microstructural evolution of CoCrFeMnNi were examined for two different grain sizes at room temperature. Microstructural investigations by transmission electron microscopy showed that, while the dislocation structures at low strain amplitude (0.3%) mainly consisted of planar slip bands, at higher strain amplitudes (0.5% and 0.7%), wavy-substructures including veins, wall, labyrinth and cells prevailed. Slip mode also changes from initially planar-slip to wavy-slip with cycle numbers. Dislocations in veins, walls, labyrinth and cells are found to have different Burgers vectors, suggesting that apart from wavy-slip, multiple-slip also contributes to their formation. Moreover, distinct dislocation substructure in grains is dictated more by the constraints from neighboring grains rather than by their orientation. Additionally, the formation of various dislocation structures in a single grain is also linked to the constraint effects from the neighboring grains.

1. Introduction

High-entropy alloys (HEAs), with single-phase solid solution, have been extensively investigated over the last 15 years [1, 2]. Among them, the equiatomic CoCrFeMnNi alloy is one of the most thoroughly studied candidates with face-centered cubic (FCC) lattice structure [3]. Due to their good combination of mechanical properties, HEAs are potential candidates for structural applications. In view of this, their fatigue performance is of crucial importance. Several studies have been carried out to shed light on the fatigue-crack growth and high-cycle fatigue behavior of equiatomic CoCrFeMnNi [4-6]. Recently, an increasing number of investigations have also been dedicated to unraveling its low-cycle fatigue (LCF) behavior [7-11]. Though these works provide important initial insights into the LCF response of CoCrFeMnNi, some of their conclusions need to be reconfirmed and several other important aspects still remain unexplored.

For instance, our previous work [10] on as-recrystallized CoCrFeMnNi suggested that dislocation substructures (*i.e.* walls, veins and cells) upon cycling are formed due to wavy-slip; however, a similar work [11] on hot-extruded CoCrFeMnNi associated wall- and cell-structure formation to planar- and wavy/cross-slip, respectively. Therefore, their formation mechanisms in terms of slip mode need further experimental clarification. Moreover, typical fatigued dislocation structures depend not only on testing parameters (*e.g.*, strain amplitude, cycle number), but also on material parameters (*e.g.*, grain orientation, grain size) [12-15]. For CoCrFeMnNi, a systematic study on the effects of strain amplitude, number of cycles and grain orientation on dislocation structures has not yet been undertaken. Furthermore, reducing grain size is usually an effective way to improve materials' fatigue performance [16, 17]. As a previous study [7] concerning the grain size effect was only limited to LCF crack initiation behavior in CoCrFeMnNi at low strain amplitudes, the investigation of the grain size effect on LCF deformation behavior for a wider strain amplitude range is deemed mandatory.

Additionally, the comparison of the LCF response of HEAs with conventional FCC steels (*e.g.*, 316L steels) having similar stacking fault energy (SFE) is of particular interest. For instance, how would their cyclic responses and microstructural evolutions differ? The answer to this question would enable an identification of features contributing to the peculiar properties of HEAs, and hence, to tune them more efficiently.

2

Consequently, the objective of this work is to systematically characterize the LCF deformation behavior of CoCrFeMnNi (including comparison to that of 316L steel) and to examine the microstructural origins of this behavior (with emphasis on effects of strain amplitudes, cycle number and grain orientation) for two different grain sizes. This LCF study may thus serve as a reference system for enhancing the understanding of the underlying fundamental deformation mechanisms in other FCC HEAs.

2. Material and experimental details

2.1 Materials

The investigated CoCrFeMnNi was synthesized from high purity elemental bulk materials (with at least 99.95 % purity). Initially, Co, Cr, Fe, Mn, and Ni elements were arc melted five times and then drop cast under pure Ar atmosphere in rod-shaped water-cooled Cu mold. Thereafter, the ingot was homogenized at 1473 K for 72 h and subsequently water-quenched. The homogenized material was then subjected to rotary swaging with which the diameter was reduced from 14 mm to 6 mm. More details about the processing of CoCrFeMnNi can be found in Ref. [18]. The miniaturized LCF specimens (gauge length: 7.6 mm; and diameter: 2 mm) were fabricated from the cold-worked rods. Before LCF tests, two batches of fabricated specimens were annealed at 1073 K and 1273 K for 1 h, respectively, to obtain a fully recrystallized microstructure with two distinct grain sizes (fine-grained (FG, ~ 6 μm) and coarse-grained (CG, ~ 60 μm)) differing by one order magnitude.

2.2 Low-cycle fatigue tests

Cyclic pull-to-push LCF-tests were carried out in air at room temperature (RT) on an MTS servo-hydraulic testing machine equipped with a 7 mm gauge length extensometer. All tests were conducted under a nominal strain rate of 3×10^{-3} s^{-1} using a symmetrical triangular waveform at different strain amplitudes ranging from 0.3% to 0.7%. Additionally, interrupted tests (up to 20 and 500 cycles) were performed for FG CoCrFeMnNi at 0.5% strain amplitude.

The number of cycles to failure or lifetime (N_f) was defined at each testing condition using the ASTM Standard E2714-13 [19]. Additionally, the inelastic strain amplitude ($\Delta\varepsilon_{in}/2$) and stress amplitude ($\Delta\sigma/2$) were determined from the hysteresis loop at half-life [10].

2.3 Microstructural characterization

Electron backscattered diffraction (EBSD) investigations were carried out using an FEI Nova scanning electron microscope (SEM) equipped with an HKL detector. For EBSD, the specimens were prepared by cutting thin strips from the gauge section of as-recrystallized/deformed samples, parallel to the loading direction (// LD), using a Well's diamond wire saw. These strips were then ground using SiC papers, and polished using diamond suspensions and finally vibratory polished using colloidal suspension of silica. All EBSD scans were acquired at an accelerating voltage of 20 kV, a working distance of 10 mm, and step size of 200 nm. The acquired EBSD data were processed and analyzed using EDAX's OIM software (version 9.0).

Transmission electron microscope (TEM) specimens were taken from the above-mentioned strips. These specimens were reduced in thickness by grinding and polishing them to about 100 µm. Thereafter, the foils were further thinned by electro-polishing using a Tenupol 5 twin-jet device. Electro-polishing was carried out using an electrolyte consisting of 10 vol% perchloric acid, 20 vol% glycerin, and 70 vol% methanol at -20 °C and 13 V. For microstructural investigations, an FEI Tecnai F20 TEM operating at an accelerating voltage of 200 kV was employed. During TEM investigations, tilting experiments were performed for imaging dislocation structures at different diffraction conditions g. Thereafter, $g \cdot b$ analysis (Table S1) was employed to determine the Burgers vector b.

3. Results

3.1 Microstructure before cyclic loading

Fig. 1a-b show representative inverse pole figure (IPF) maps for the investigated CoCrFeMnNi after annealing at 1073 K and 1273 K, respectively. As evident, at both conditions CoCrFeMnNi exhibits equiaxed grains with a high density of annealing twins and no significant texture. The average grain sizes at two annealing conditions were determined to be ~ (6 ± 3) µm and ~ (60 ± 30) µm, respectively (see insets of Fig. 1a-b). These two variants are termed hereafter FG and CG CoCrFeMnNi, respectively. Besides, at both conditions CoCrFeMnNi bears a low dislocation density (*e.g.,* see TEM bright-field (BF) micrograph in Fig. 1c for FG material).
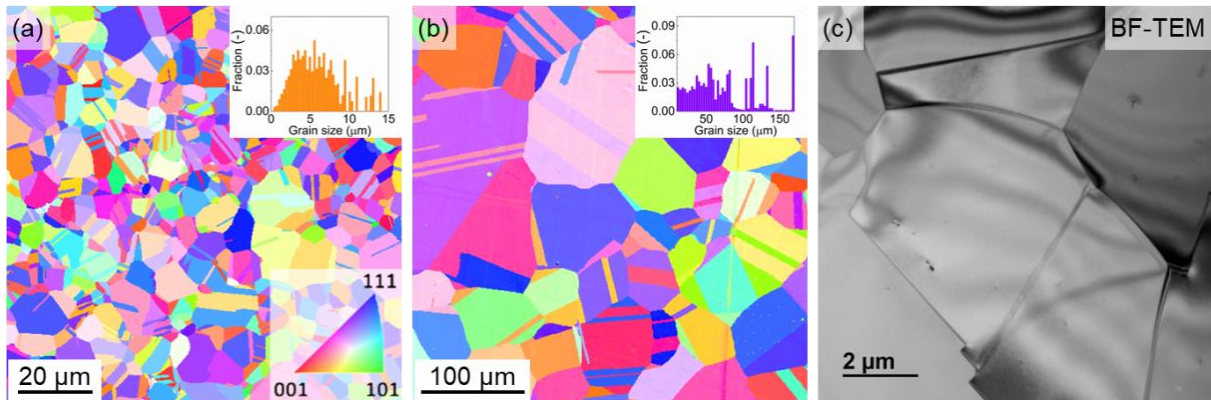
Fig. 1. Microstructure of CoCrFeMnNi annealed at (a) 1073 K [10] and (b) 1273 K. Figures (a) and (b) are representative IPF maps acquired via EBSD along the swaging direction. The grain size distributions of each state are provided in the insets. Figure (c) is a representative TEM-BF micrograph illustrating low initial dislocation density after 1073 K annealing.

3.2 Cyclic response and fatigue lifetime

The cyclic response of both materials is displayed in Fig. 2a-b, where tensile peak stress and inelastic strain amplitude are plotted against the normalized number of cycles (N/N_f), respectively. Similar curves showing these evolutions with the number of cycles can be found in the supplementary material (Fig. S1a-b). As shown in Fig. 2a, both materials in general bear a similar cyclic stress response. Initially, the tensile peak stresses increase rapidly (cyclic hardening), followed by their rapid decrease (cyclic softening) and, finally, minor changes in their level (with either minor softening for CG or 'near-steady state' for FG counterpart) are observed until failure (crack nucleation and propagation). Also evident, the majority of the lifetime is occupied by a stage with minor change in the stress levels. With respect to the influence of the applied strain amplitude, the rate and amount of initial hardening both increase with increasing strain amplitude. Furthermore, there is an indication of secondary hardening after the near-steady state at the highest applied strain amplitude (0.7%) for the FG sample (Fig. 2a and Fig. S1a). In comparison, FG material shows a higher cyclic strength and a lower cyclic hardening than the CG material (Fig. S1a). The amount of cyclic hardening is determined to be ~30-80 MPa and ~80-150 MPa for FG and CG materials, respectively (see Fig. S1a).

5
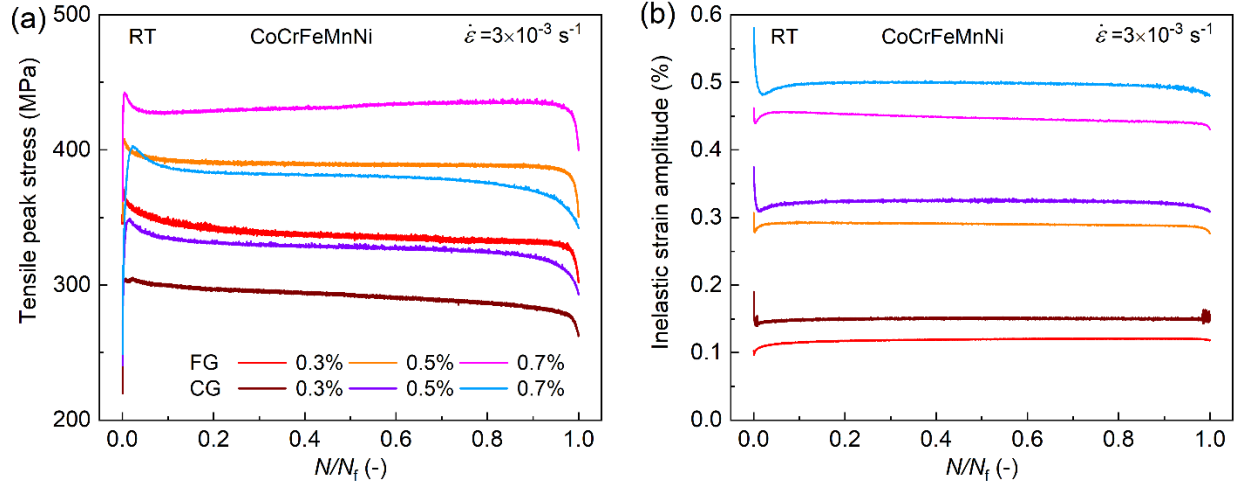
Fig. 2. (a) Tensile peak stress, and (b) inelastic strain amplitude *versus* normalized number of cycles (N/N_f) curves for FG [10] and CG CoCrFeMnNi under different strain amplitudes at RT. The color bar in (a) is also valid for (b).

Consistent with the variation of peak stresses, the inelastic strain amplitudes in Fig. 2b exhibit an initial rapid decrease followed by a gradual increase and near saturation stage until failure. Moreover, the inelastic strain amplitudes of FG material are lower than those of the CG material. The lower inelastic strain in FG material is related to its higher elastic strain due to its higher cyclic/yield strength, as compared to CG material (see half-life hysteresis loops in Fig. 3a).

The relation between the saturated stress amplitude $\Delta\sigma/2$ and inelastic strain amplitude $\Delta\varepsilon_{in}/2$ could be expressed by a power-type relation ($\Delta\sigma/2 = K'(\Delta\varepsilon_{in}/2)^{n'}$ [20], where K' is the cyclic strength coefficient and n' is the cyclic work hardening exponent). The corresponding data as well as fitted curves/parameters for both grain sizes at half-life are plotted in Fig. 3b, which suggests a fairly linear relation between the saturation stress and inelastic strain amplitude at log-log scale.
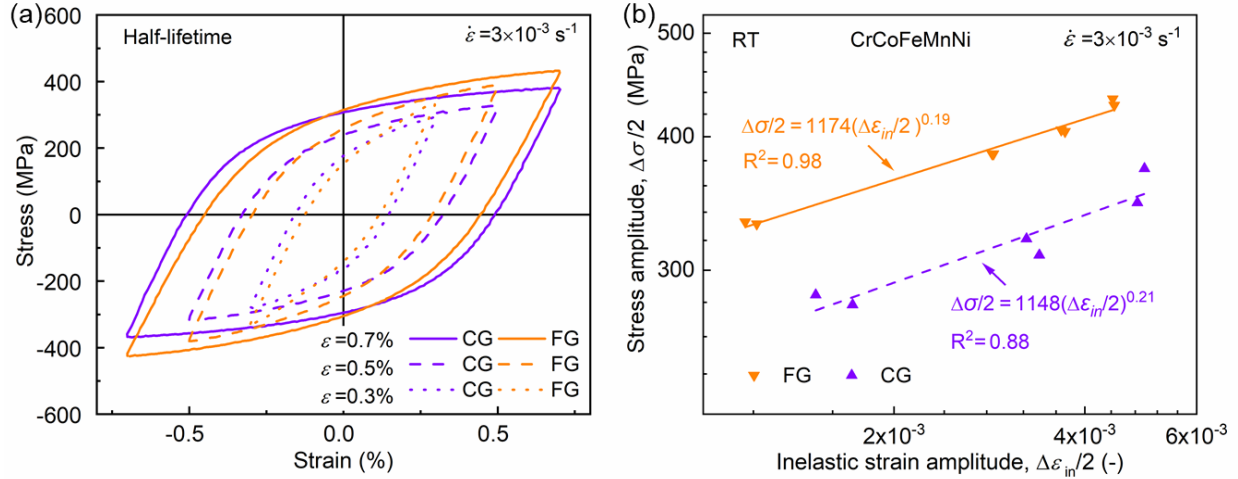
Fig. 3. (a) Typical hysteresis loops at half-life and (b) the stress amplitude (Δσ/2) *versus* inelastic strain amplitude (Δε$_{in}$/2) plot of FG [10] and CG CoCrFeMnNi at RT.

Fig. 4a shows the Δσ/2 *versus* N_f plot for both FG and CG CoCrFeMnNi. Evidently, at similar Δσ/2, the FG material exhibits a longer lifetime than the CG material, indicating a better cyclic stress resistance with grain refinement. Fig. 4b presents Δε$_t$/2 *versus* 2N_f plot. Though experimental scatter convolutes the comparison, the FG material's higher fatigue life is still apparent for a given total strain amplitude when compared to the CG counterpart (Fig. 4b). In Fig. 4c, the Δε$_{in}$/2 *versus* 2N_f plots for both grain sizes are shown, lying almost on top of each other (fitted by Coffin-Manson curve, $\Delta\varepsilon_{in}/2 = \varepsilon'_f (2N_f)^c$ [21, 22]). The fitted parameters are present in Fig. 4c. Similar fitted curves/parameters suggest their grain size independence within the investigated micrometer range. This is related to the lower induced inelastic strain in the FG material when compared to its CG counterpart at a given strain amplitude (Fig. 3a).
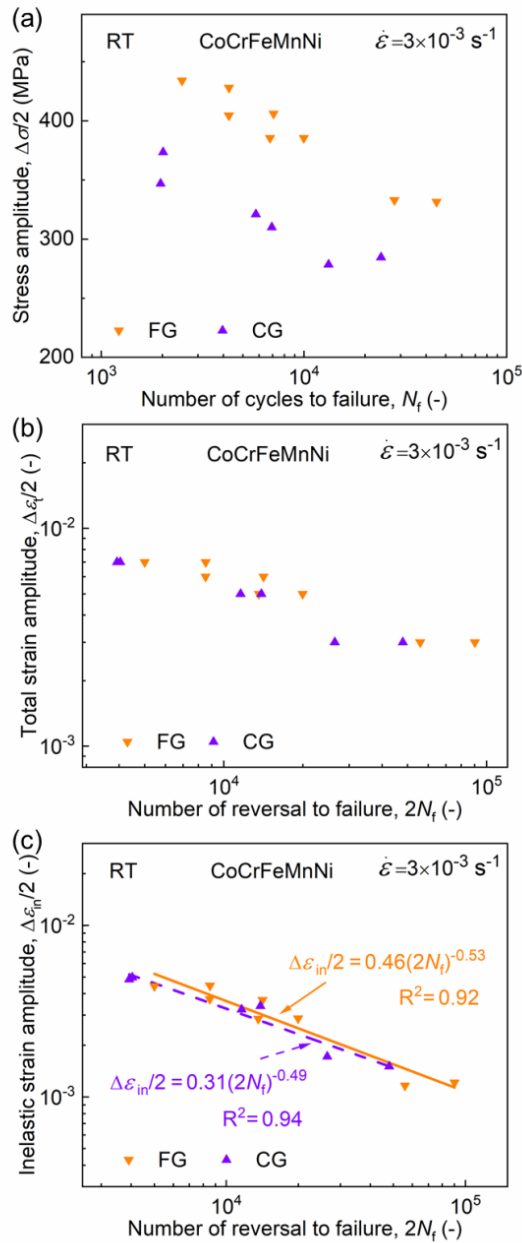
Fig. 4. Plots of (a) stress amplitude ($\Delta\sigma/2$) *versus* number of cycles to failure (N_f), (b-c) total and inelastic strain amplitude ($\Delta\varepsilon_t/2$, and $\Delta\varepsilon_{in}/2$) *versus* number of reversals to failure ($2N_f$), respectively, for FG [10] and CG CoCrFeMnNi.

3.3 Microstructure after cyclic loading

In general, post-fatigued EBSD investigations for both materials showed no significant change in texture, average grain sizes and twins fractions in comparison to the annealed states (*e.g.*, see

8

Fig. S2). Nevertheless, more detailed TEM investigations on both materials reveal a high density of dislocations with distinct configurations as well as occasional deformation twinning.

3.3.1 Microstructure upon cycling at 0.3% strain amplitude

Fig. 5 presents TEM-BF micrographs of the post-fatigued FG samples tested at 0.3% strain amplitude. Planar slip bands (SBs) are recognized to be the main deformation-induced microstructural features (Fig. 5a-e). As evident in Fig. 5a-c, a high dislocation density is observed. The dislocations are arranged on {111} planes inside bands, surrounded by apparently dislocation-free regions. In some SBs, dislocations are proven to be dipoles having +*b*/-*b* Burgers vectors (see Fig. 5a, and enlarged images in Fig. 5d-e). The dipole character of the dislocation pairs was confirmed by performing tilting experiments using +*g*/-*g* diffraction conditions according to [23-25].

Additionally, as shown in Fig. 5c, individual dislocations in other SBs (with the same Burgers vector) form pile-ups against grain boundaries (GBs). Apart from planar dislocation structures, dislocation walls are occasionally observed (Fig. 5f).
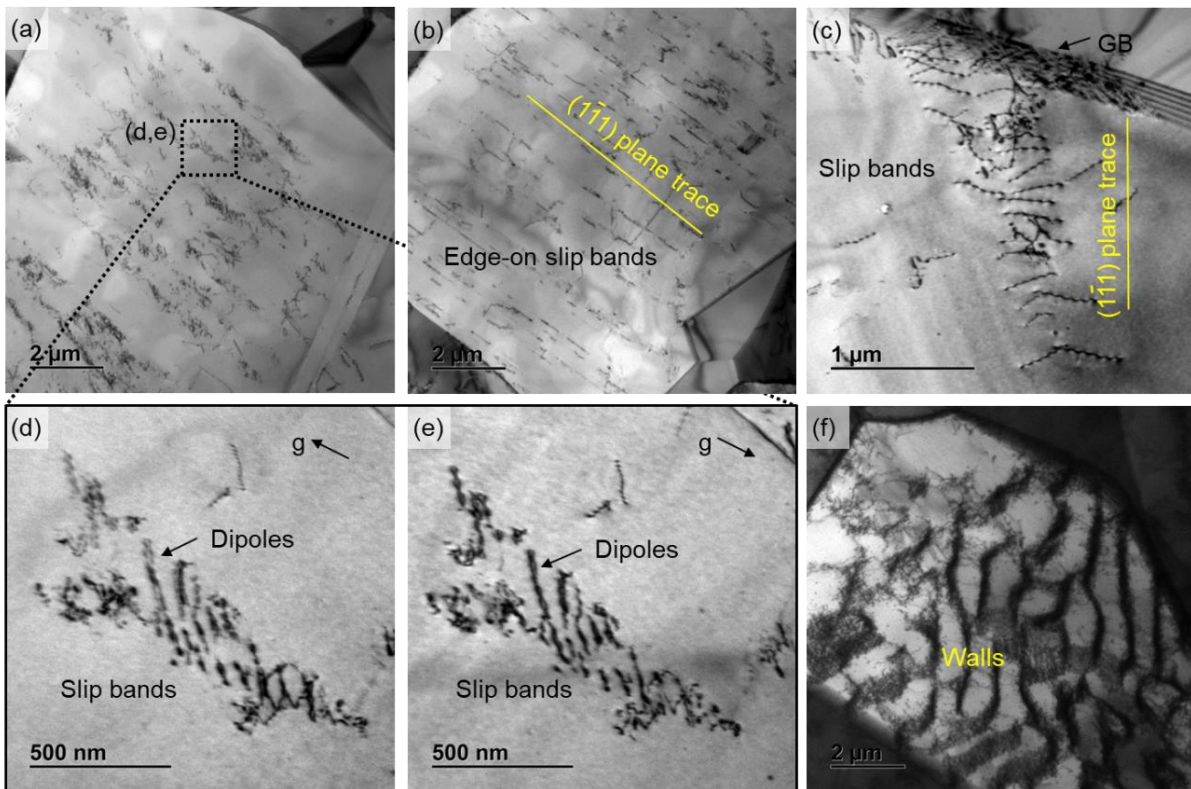
Fig. 5. TEM-BF micrographs revealing dislocation structures in FG CoCrFeMnNi tested at 0.3% strain amplitude until failure. Planar SBs are the main observed microstructural features. (a-e) Planar SBs consisting of dislocations with (c) the same Burgers vector, and (d-e) a pair of opposite Burgers vectors (*i.e.*, dipoles, indicated by the altered distance between two dislocations by reversing the *g* condition). (f) Dislocation wall structure.

3.3.2 Microstructure evolution upon cycling at 0.5% strain amplitude

Fig. 6 presents TEM-BF micrographs of a FG sample tested at 0.5% strain amplitude until failure. In general, due to the higher induced inelastic strain than 0.3% strain amplitude, significantly higher densities of dislocations are observed. Furthermore, the planar dislocation arrangements became less frequent and well-developed dislocation substructures, such as parallel walls, irregular veins and cells, became more prevalent (Fig. 6a-c).
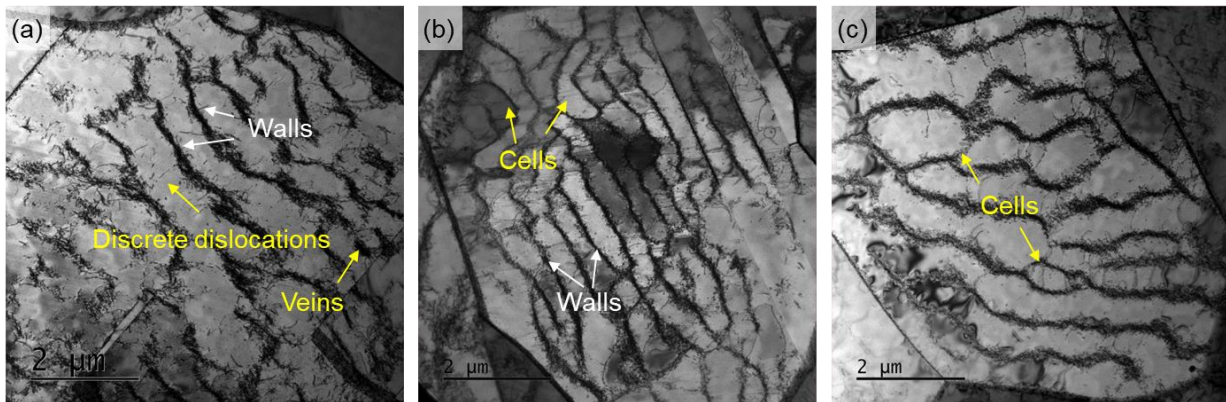
Fig. 6. TEM-BF micrographs revealing dislocation structures in FG CoCrFeMnNi tested at 0.5% strain amplitude until failure. Well-defined dislocation substructures, such as parallel walls, irregular veins and cells are prevalent. (a) Wall and vein structures. (b) Wall and cell structures. (c) Cell structures.

To establish how dislocation structures evolve at different cyclic stages, additional TEM investigations were performed on FG specimens that were interrupted at the 20th and 500th cycles, corresponding to cyclic hardening and softening stages, respectively.

Fig. 7 shows TEM micrographs of a FG specimen fatigued up to 20 cycles. As evident, dislocations are mainly arranged in the form of tangles (Fig. 7a-b) and planar SBs (Fig. 7c-f). Using different two-beam diffraction conditions, dislocations in tangles are found to have different *b*. For instance, from *g·b* analysis (Table S1), the marked dislocations in Fig. 7a-b are

perfect dislocations with **b** ½[0$\overline{1}$1], while others have different **b**, suggesting multiple-slip systems activation.

Planar SBs are found to consist of arrays of full dislocations with **b** ½[0$\overline{1}$1] on the primary slip system (see dislocations indicated by white arrows in Fig. 7c). Additionally, the dislocations indicated by black arrows in Fig. 7c have the same **b** ½[0$\overline{1}$1]. Since the parts of these dislocations (black arrows in Fig. 7c) are approximately parallel to the direction of **b** (see the yellow arrow), these portions are of screw nature, which is an indication of cross-slip. In other planar SBs, dislocations are found to be dipole pairs (Fig. 7d-e).

Lastly, partial dislocations with narrow stacking fault (SF) in between are sporadically recognized by weak-beam dark-field technique (*e.g.*, see Fig. 7f). It is noteworthy that the above-mentioned dislocation substructures (*i.e.*, walls, veins and cells) were not observed at this stage.
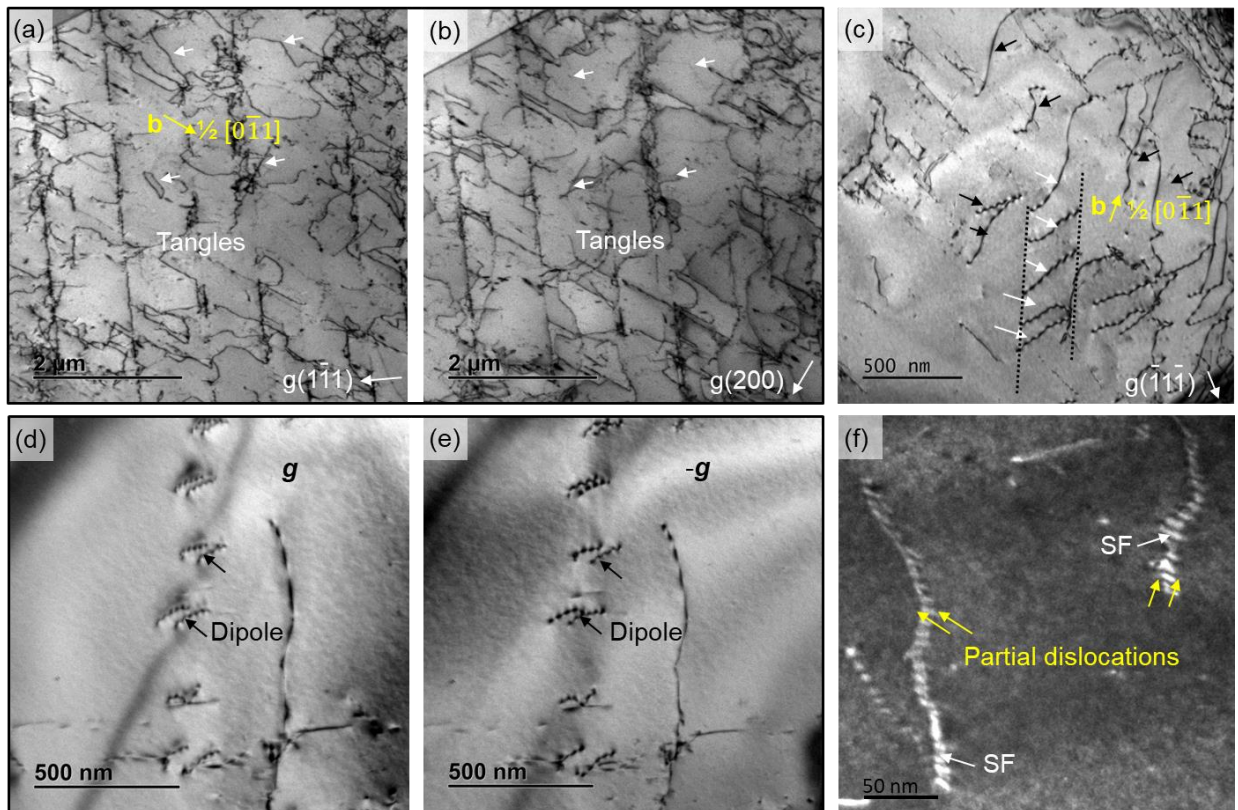
Fig. 7. TEM micrographs revealing dislocation structures in FG CoCrFeMnNi tested at 0.5% strain amplitude after 20 cycles, representing cyclic hardening. Dislocation tangles and planar slip bands are common features. (a-b) Multiple-slip systems activated dislocations and tangles. (c-f) Planar slip bands,

consisting of (c) primary dislocations, (d-e) dislocation dipoles, and (f) occasionally partial dislocations co-existing with narrow SFs.

Fig. 8 presents the microstructure of the FG specimen which was interrupted at 500 cycles. At this stage, dislocations rearranged into substructures, such as veins and walls. Nevertheless, in comparison to the well-defined dislocations substructures observed at the end of the lifetime (Fig. 6), these structures are relatively ill-defined (*e.g.*, top right corner of Fig. 8a, and right side of Fig. 8b). By using **g·b** analysis, dislocations in ill-defined walls and veins are found to have different **b** (see enlarged Fig. 8d-f, where walls and veins are simultaneously visible under $1\bar{1}1, \overline{1}\overline{1}1, \bar{2}00$ diffraction conditions), which suggests domination of multiple-slip. In-between walls or veins (*i.e.*, in channels), only few single dislocations are observed. These discrete dislocations were identified to be of screw type, such as ½[$0\bar{1}1$] primary dislocations (indicated by white arrows in Fig. 8d-f). Besides, partial dislocations along with SFs are still occasionally observed (*e.g.*, see Fig. 8c).
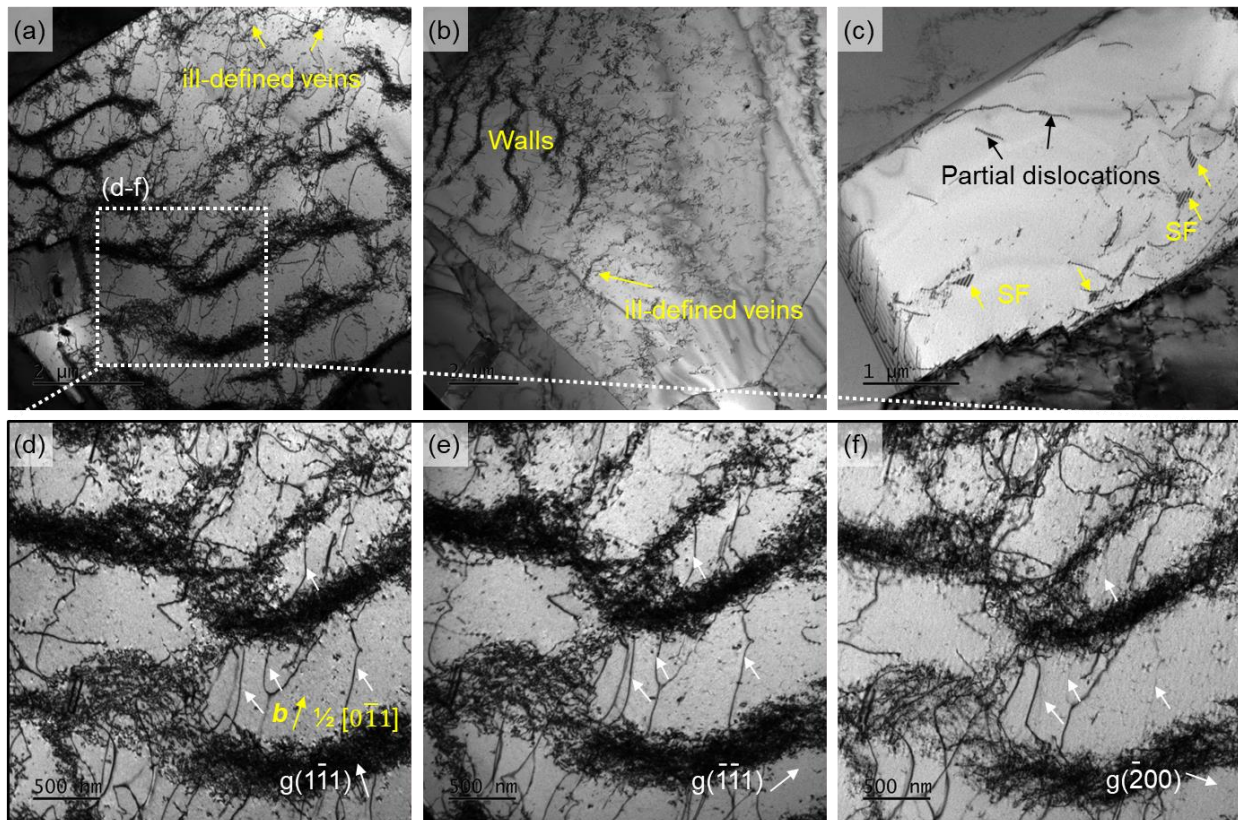
Fig. 8. TEM-BF micrographs revealing dislocation structures in FG CoCrFeMnNi tested at 0.5% strain amplitude after 500 cycles representing cyclic softening stage. Ill-defined dislocation substructures are dominant in this stage. (a-b) Ill-defined wall and vein structures. (c) Sporadically observed partial

dislocations and SFs. (d-f) Dislocations in the walls having different Burgers vector, and those in the channels having screw character confirmed by micrographs taken at three different two-beam diffraction conditions.

3.3.3 Microstructure upon cycling at 0.7% strain amplitude

Fig. 9 shows typical dislocation structures in post-fatigued FG CoCrFeMnNi tested at 0.7% strain amplitude. Similar to 0.5% strain amplitude, well-developed substructures (including wall, vein, cell and labyrinth structures) are the main microstructural features (Fig. 9a-f). However, at 0.7% strain amplitude, these structures appear to be more condensed (indicating an increase of dislocation density), labyrinth and cell structures appear to become more prominent as well.
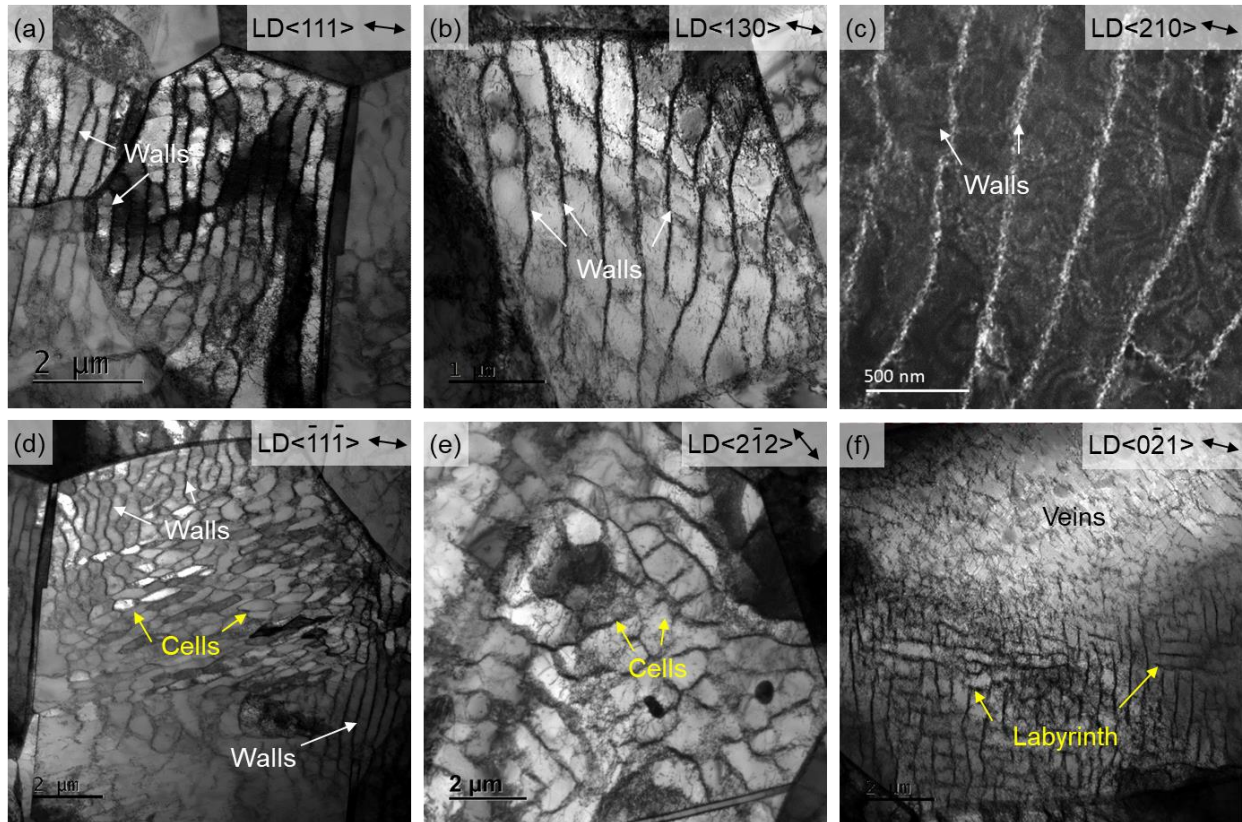
Fig. 9. TEM micrographs revealing the dislocation structures in FG CoCrFeMnNi tested at 0.7% strain amplitude until failure. Well-developed substructures (*i.e.,* walls, veins, cell and labyrinth) are the main dislocation features. (a-c) Wall structures. (d) Wall and cell structures. (e) Cell structures. (f) Labyrinth and vein structures.

Furthermore, the grain orientation dependence of distinct dislocation substructures was investigated for FG CoCrFeMnNi tested at 0.5% and 0.7% strain amplitudes. Apart from some

expected observations (*e.g.*, a similar type of dislocation structures was formed in grains with similar orientations, not shown here), other unexpected results can be summarized as follows: (i) In grains with similar orientations, dislocations were rearranged into different substructures. For instance, as shown in Fig. 9a and Fig. 9d, dislocations in grains oriented in <111> parallel to the loading direction (// LD) were arranged in parallel wall and cell structures, respectively. (ii) The same type of dislocation structure was occasionally formed in grains of different orientations. For example, as in Fig. 9a-c, a wall structure was observed in grains with the <111>, <120> and <130> directions // LD, respectively. (iii) In a single grain, various dislocation structures were observed. For instance, walls, veins and cells coexisted in a same grain (Fig. 9d). Additionally, no preferred orientation for specific dislocation structure formation was noticed for samples tested at a low strain amplitude of 0.3%. These results suggest no significant relation between grain orientation and distinct dislocation structure. This is discussed in more detail in section 4.3.

3.3.4 Microstructure upon cycling coarse-grained CoCrFeMnNi

In general, CG material exhibits similar microstructural evolution as FG material. Dislocation substructures (*i.e.*, wall, vein and labyrinth structures) developed in CG CoCrFeMnNi tested at a strain amplitude of 0.7% are shown in Fig. 10. Besides, ladder-like persistent slip-band (PSB) structures are also apparent (Fig. 10b). TEM micrographs, acquired at three different ***g*** conditions (not shown here), confirmed that dislocations in the ladder's rung also have different ***b***. Additionally, in CG material, different dislocation structures formed in a single grain more frequently (Fig. 10). In such a manner, larger plastic strain can be accommodated in a single grain, which could be related to the CG material's shorter fatigue life (Fig. 4).
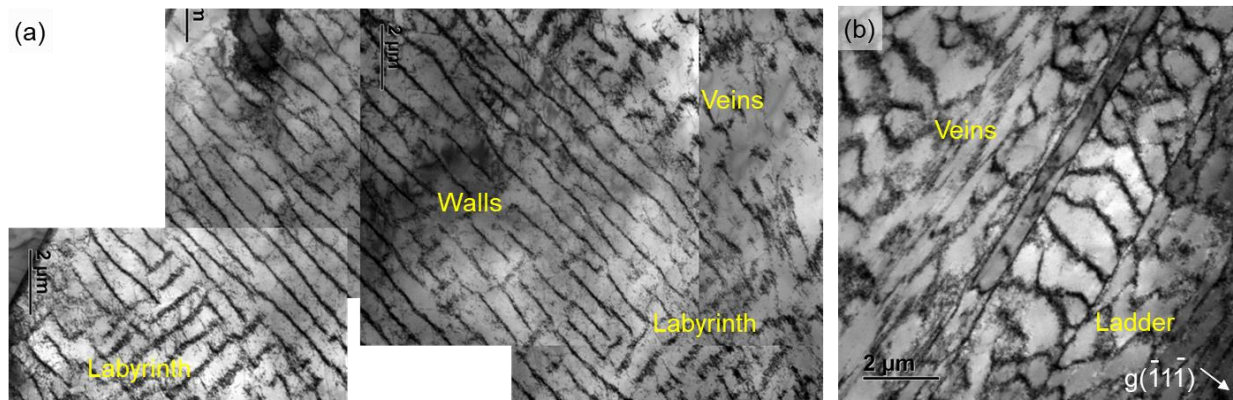
Fig. 10. TEM-BF micrographs revealing dislocation structures in CG CoCrFeMnNi tested at 0.7% strain amplitude until failure. (a) Various dislocation structures (walls, veins and labyrinth) formed in a single grain. (b) Ladder-like PSB structures containing dislocations with different Burgers vector.

Furthermore, as a peculiar feature of CG CoCrFeMnNi at 0.7% strain amplitude, the deformation twinning (DT) in few near <111> // LD oriented grains was observed, see Fig. 11. Since the CG sample tested at 0.7% strain amplitude manifests mainly dislocation substructures (Fig. 9) maintaining the trend of the cyclic stress response at other conditions (Fig. 2), the presence of DT appears to have no significant influence on the mechanical response. Contrary to the above observation for CG material, no DT was observed in FG samples.
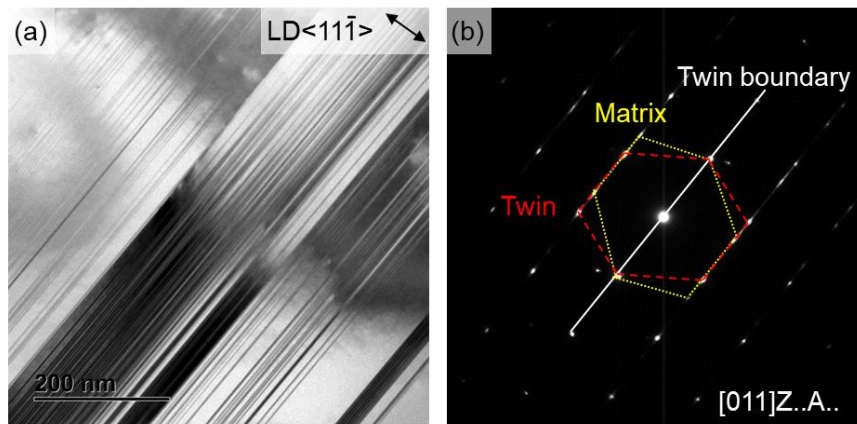
Fig. 11. (a) TEM micrograph coupled with the corresponding (b) selected area diffraction pattern taken along a [011] zone axis, revealing deformation twinning for CG CoCrFeMnNi tested at 0.7% strain amplitude until failure.

4. Discussion

4.1. Influence of strain amplitude on microstructure

It is known that the microstructural evolution upon cycling depends on the applied strain amplitude. In the present investigations, at a low strain amplitude of 0.3%, planar SBs, in some cases along with dislocation dipoles, are predominantly observed (Fig. 5). The formation of dipoles is related to the loading on reversal that may activate dislocation sources in the opposite directions [26]. These dislocation structures suggest that at low strain amplitudes, CoCrFeMnNi deforms by planar single-slip, consistent with that observed at low strains under monotonic loading [27]. The planar slip is attributed to the material's low-to-medium SFE [27]. Of interest to note is that the local chemical short range ordering (SRO), if existent, could also promote planar

slip [28, 29]. However, in CoCrFeMnNi, there has been no strong indication of SRO so far. Instead, one of its subset, CoCrNi, has shown more potency for SRO based on ab initio estimations [30, 31], but this also has only been observed after prolonged annealing at 1000 °C for 120 h, followed by slow cooling [32]. In the present study, all heat treatments carried out were of a shorter duration (1 h) and more importantly, all samples were quenched to room temperature. Thus for the investigated CoCrFeMnNi alloy, it can be concluded that SRO is either non-existent or negligible.

Contrarily, at both intermediate and high strain amplitudes, dislocation-rich regions (*i.e.*, walls, cells, labyrinth and veins) separated by dislocation-depleted regions (*i.e.*, channels) are typically observed (Fig. 6, Fig. 9 and Fig. 10). Among these structures, wall and ladder structures have similar morphology as PSBs [12, 33-39]. These PSB-walls have been reported to originate from the metastable veins structure [40]. The formation of edge-multipole veins can be attributed to the effective elimination of screw dislocations by extensive cross-slip. Therefore, the wavy-slip mode, characterized by easy cross-slip, favors the formation of the metastable veins and their transformation into PSBs. Besides, veins and walls are reported to mainly contain full dislocations with the same *b* [35]. However, in the present study, veins and walls consist of dislocations with different *b* (see, Fig. 8d-e). Consistent with a previous report [41], this observation indicates that apart from the cross-slip, multiple-slip system activation also contributes to the formation of walls and veins.

Additionally, it has also been well-accepted that easy cross-slip and multiple-slip are essential prerequisites for the formation of cell and labyrinth structures [35, 41]. Consistently, our results reveal that multiple-slip (including cross-slip) contributes to their formation. Furthermore, labyrinth and then cell structures have been considered to transform from wall structure [42]. Since our results confirm that all of them originate from multiple-slip (including cross-slip), it is reasonable to conclude that dislocation walls are also metastable structures which upon further loading could transform into labyrinth and then cell structures. Indeed, at higher strain amplitude (0.7%), more frequent labyrinth and cell structures were observed. Together, these results suggest that increasing strain amplitude leads to a transition of slip mode from planar-slip (*i.e.*, slip bands) to wavy-slip (*i.e.*, walls, veins, labyrinth and cells) in CoCrFeMnNi.

Cumulative inelastic strain (*i.e.*, $\varepsilon_{cum} = 4\ \varepsilon_{in} \cdot N_f$) and dislocation configurations are typically interrelated. For both FG and CG materials, ε_{cum} was calculated and plotted against applied strain amplitude in Fig. 12. Due to the highest number of cycles to failure observed at the lowest

applied strain amplitude (0.3%), ε_{cum} is largest, and it decreases with increasing strain amplitude. Furthermore, due to higher fatigue life, FG material also manifests higher ε_{cum} than CG material at each investigated strain amplitude. Another interesting observation is that no prominent dislocation substructure is formed at the low strain amplitude of 0.3%, despite the highest ε_{cum}. This is because planar single-slip, which is more or less reversible, is more dominant at 0.3% strain amplitude, whereas, due to the activation of multiple-slip (including cross-slip) at higher strain amplitudes, dislocation interactions (including their annihilation) lead to the formation of dislocation substructures. Therefore, these observations indicate that the saturated dislocation structures are more related to the applied strain amplitude rather than to the ε_{cum}.
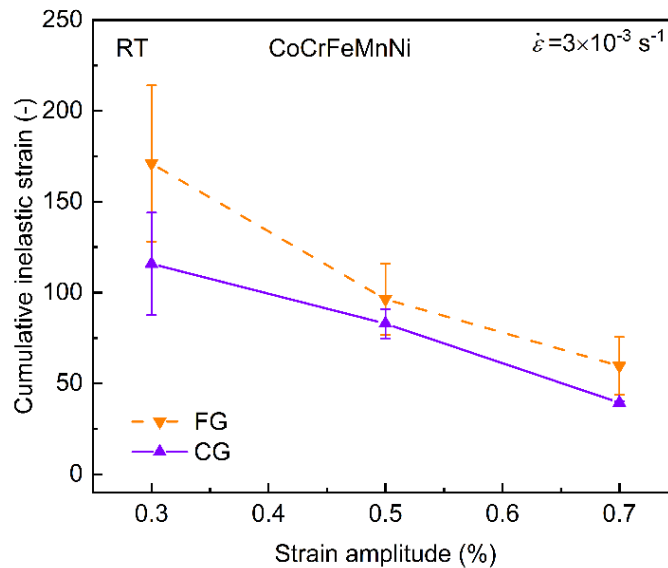
Fig. 12. The cumulative inelastic strain of FG and CG CoCrFeMnNi is plotted against strain amplitude. The lines are guidelines to the eye, only.

Apart from the distinct dislocation structures, DT is sporadically observed in grains with their <111> axis along the loading direction of CG CoCrFeMnNi when the highest strain amplitude (0.7%) was applied. Contrarily, no DT was observed in FG samples, despite a higher stress level at similar testing conditions. The likely reason lies in the fact that the critical stress required for twinning (CTS) is grain-size dependent [43]. Laplanche et al. [44] obtained an experimental CTS value of 720 ± 30 MPa for CoCrFeMnNi with ~16 μm grain size. Although the experimental CTS values for the investigated grain sizes are not yet available, our results suggest that the CTS must have been achieved upon cycling for the CG CoCrFeMnNi, while not for the FG version. Nonetheless, it is noteworthy that due to the limited volume fraction of DT, they should have a

17

minor contribution in accumulating inelastic strain; and hence, in governing fatigue properties of CoCrFeMnNi in the investigated straining regime.

4.2. Influence of cycle number on dislocation structures

In order to reveal the evolution of dislocation structures during cyclic straining and to correlate it with the observed cyclic stress response, LCF tests at 0.5% strain amplitude were interrupted at different cyclic stages. During the initial cycles, dislocations nucleate/multiply and spread across grains via planar single-slip (*e.g.*, SBs). Otto et al. [27] also reported planar single-slip to dominate at small strains under monotonic loading at RT (*e.g.*, up to 2.1%). Here, dislocation multiplication and interaction with solute atoms contribute to the increased flow stress (*i.e.*, cyclic hardening). As the flow stress increases, the secondary/multiple-slip systems are activated, which leads to the formation of dislocation tangles (see Fig. 7a-b acquired from a fatigued specimen interrupted after 20 cycles). The curved morphology of dislocations in Fig. 7a-b and the measured ***b*** for dislocations in two slip bands in Fig. 7c, give indications of their wavy/cross-slip behavior. Therefore, it can be concluded that slip is initially planar but it quickly expands to wavy-slip which is the dominant slip mode for the entire lifetime.

Upon further cycling (*e.g.*, at 500 cycles, corresponding to softening stage), dislocations from multiple-slip systems (*i.e.*, tangles) rearrange into dislocation-rich ill-defined walls and veins (Fig. 8) to minimize stored dislocation strain energy [45, 46]. In dislocation-depleted channels, discrete dislocations are found to have predominant screw character (Fig. 8a, d-f), consistent with previous findings on FCC metals [35]. As these screw dislocations can glide or cross-slip, they could mutually annihilate with dislocations of opposite ***b*** and deposit edge segments along the walls [47]. The screw dislocation motion is also envisioned to shuttle forward and backward upon cycling and carry most of the imposed plastic strain [26, 47]. Therefore, the increased mean free path (*i.e.*, in channels) for dislocation movement contributes to the cyclic softening.

With further cycling (*i.e.*, at near steady state), dislocations continue to rearrange into high-density regions, leading to the formation of well-developed substructures in most grains (Fig. 6). The near saturation of the dislocation density, resulting from a dynamic equilibrium between dislocation multiplication and annihilation, contributes to a minor change in the flow stress until failure [34, 35, 48].

Based on similar observations for a post-fractured FG sample tested at 0.7% strain amplitude (Fig. 8), it is reasonable to conclude that a similar microstructural evolution applies for samples

tested at high strain amplitudes. The secondary hardening for a FG sample tested at 0.7% (Fig. 2a) can be associated with the substantial transformation of walls into more prominent labyrinth and cell structures, which decreases the mean free path of dislocation movement.

Additionally, for the sample tested at low strain amplitude (*e.g.*, 0.3% with planar slip domination, see Fig. 5), the microstructural evolution is different from that at 0.5% strain amplitude. It could be expected that dislocation multiplication and interaction (mainly along with solutes) contribute to the initial cyclic hardening. Upon further cycling, dislocations (*i.e.*, dipoles) in the planar SBs move and annihilate, leading to cyclic softening. Thereafter, as the dislocation density reaches a quasi-stable state, the flow stress tends to saturate until failure.

4.3. Influence of grain orientation on dislocation structures

For microstructural based modeling, the type of dislocation structure formation based on grain orientation is of particular interest. It is well-known that for FCC single crystals (*e.g.*, copper, nickel), PSB-wall and labyrinth structures dominate in near [011] and [001]-oriented grains (// LD), respectively [49], while in near [$\bar{1}$11]-oriented grains, vein and cell structures are found at low and high strain amplitudes, respectively [49, 50].

In the present study, for polycrystalline CoCrFeMnNi, no significant correlation between dislocation patterns and grain orientations was observed. This could be related to the different amount of constraint effects from the distinctly different neighboring grains environment. For instance, at medium and high strain amplitudes, different slip systems are activated within a grain to maintain strain compatibility across the GBs. For grains with similar orientations, their neighboring grains orientation might be distinctly different, which could impose a different amount of constraint effects leading to the development of different dislocation structures (Fig. 9d).

Moreover, the amount of constraint effects within a single grain may also vary (especially for coarse grains). As illustrated in Fig. 13a, the region 1 and 2 may experience a different amount of constraint effects because of different neighboring grains orientation, which gives rise to the formation of wall and cell mixed structures in a single grain (see similar micrograph as Fig. 9d). Specifically, the larger amount of constraint effects (*e.g.*, in region 2) could promote walls to transform into cell structure. However, this interpretation is not in agreement with the rationalization provided in Ref. [11]. The authors ascribed the development of cell and wall structures in a single grain of CoCrFeMnNi to the activation of cross/wavy-slip and planar-slip,

respectively. Their rationalization is based on the description by Copley and Kear [51], *i.e.*, that reversing the sign of applied stress leads to the change of Shockley partial separation distance (and hence 'effective' SFE) for certain orientations and thus might cause a change in the dislocation slip mode [51]. To validate this rationalization, the orientations for the grains showing cell/wall/mixed structures in the present study are plotted in the color-coded IPFs, see Fig. 13b-c. The connecting line between [102] and [113] directions separates the regions of extension or contraction of stacking faults confined by the partial dislocations illustrated by the difference in Schmid factors on the partials (provided for tension; in compression the sign reverses). The anisotropy becomes more pronounced with increasing distance from this line (hence, significant change between wavy/planar slip during load reversal). Since no systematic trend of grain orientations was found for either of the assigned structures in Fig. 13b-c, and all dislocation structures were confirmed to be originating from multiple-slip (including cross-slip, see section 4.1) rather than the planar-slip, it is suggested that the formation of mixed structures in a single grain is dictated by the constraint effects of neighboring grains.
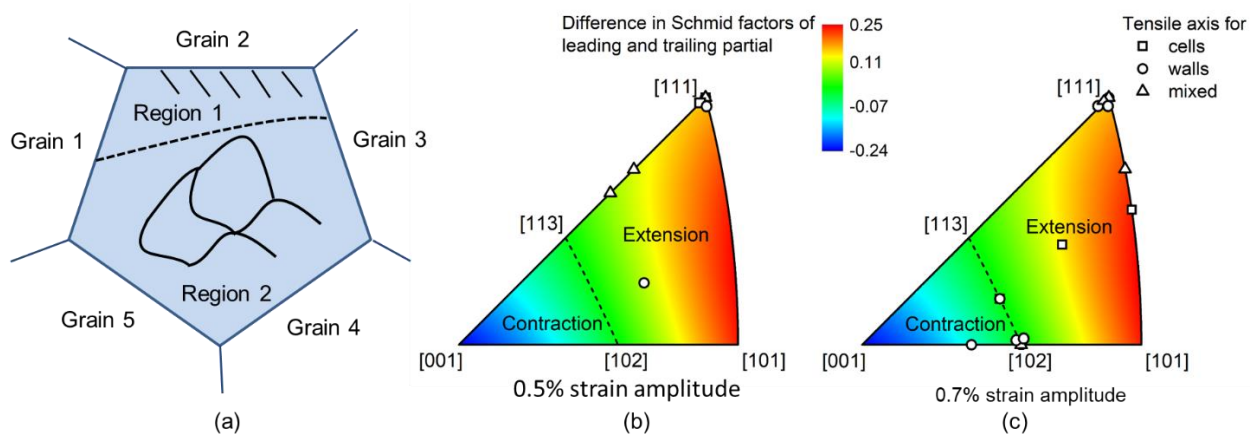
Fig. 13. (a) The schematic illustration of mixed (cells and walls) structures formation in a single grain due to different amount of constraint effects from neighboring grains. (b-c) The color-coded IPFs showing orientations for the grains with cell/wall/mixed structures, were obtained from FG samples tested at 0.5% and 0.7% strain amplitudes, respectively. The line between [102] and [113] separates the regions of extension or contraction of partial dislocations (provided for tension; in compression the sign reverses).

No significant relation between grain orientation and dislocation structures for CoCrFeMnNi is consistent with those observed for other FCC polycrystalline materials (*e.g.*, copper, 316L steel), where various dislocation patterns were observed in grains with similar orientation or a single grain [37, 41]. In contrast, a study on fatigued polycrystalline nickel [52] reported that the

dislocation patterns, observed via electron channeling contrast imaging (ECCI), are similar to that for a single crystal with same orientation. This discrepancy may arise from the fact that, though ECCI could provide a larger overview of microstructures, its resolution is not as high as TEM to differentiate between cell and wall (or vein) structures. Indeed, a later study on fatigued polycrystalline nickel [53] showed various dislocation structures (walls and cells) in a single grain via TEM, which is consistent with the present investigations.

4.4. Comparison to 316L austenitic steel

Upon cycling, CoCrFeMnNi exhibits similar dislocation structure evolution as observed for 316L austenitic steel [12, 13]. This can be rationalized by their similar SFE (CoCrFeMnNi: 30 ± 5 mJ/m^2 [54] and 316L steel: ~28 mJ/m^2 [55]), as it is known to strongly influence the dislocations slip mode [10, 56]. It could also be concluded that such a dislocation evolution is also applicable for other FCC HEAs and their subsets with similar SFE.

Considering the similarities between the 316L steel and CoCrFeMnNi, the comparison of their cyclic response is of importance. Fig. 14 presents the hysteresis loops of CG CoCrFeMnNi and 316L steel (average grain sizes ~60 µm, taken from [57]) tested under 0.7% strain amplitude (at 2nd and 31st cycles) at RT. Note that the 31st cycle corresponds to the end of cyclic hardening stage for both materials. As evident, at 2nd cycle, both materials show similar inelastic strain (*i.e.* width of the hysteresis loop at zero stress). At 31st cycle, due to cyclic hardening, both materials exhibit a decrease in inelastic strain. However, in comparison to 316L steel, CoCrFeMnNi shows a lower inelastic strain. Therefore, it is expected that CoCrFeMnNi would have a longer lifetime than 316L steel at the same total strain and stress conditions. The lower inelastic strain in CoCrFeMnNi results from its associated higher yield stress (see peak stresses at the 2nd cycle) and cyclic hardening ability (see peak stresses at the 31st cycle), stemming from larger solid solution strengthening. This suggests that CoCrFeMnNi or its subsets with higher strength and sufficient ductility could be good candidates with better LCF resistance compared to conventional FCC steels (*e.g.*, 316L steel) in safety-critical engineering applications. For more accurate inelastic strain *versus* lifetime comparison, similar LCF tests would be needed for 316L steel, which is beyond the scope of this work.
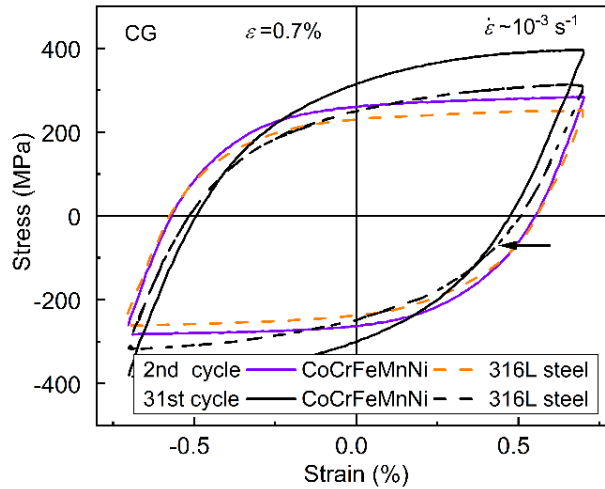
Fig. 14. Hysteresis loops of CG CoCrFeMnNi and 316L steel (average grain sizes ~60 μm) [57], which are tested at RT under 0.7% strain amplitude, at the 2nd and 31st cycles, respectively.

5. Conclusions

In the present work, low-cycle fatigue (LCF) behavior of CoCrFeMnNi HEAs with two different grain sizes, ~6 μm and 60 μm, was investigated at different strain amplitudes ranging from 0.3% to 0.7%. Extensive TEM investigations were carried out to unravel microstructural origins of the deformation behavior. The key findings are summarized as follows:

(1) Reducing the grain size to a few micrometers leads to an enhanced LCF lifetime for CoCrFeMnNi at the investigated strain amplitudes.

(2) The dislocation structure mainly consisted of planar slip bands at low strain amplitude (0.3%); while at larger strain amplitudes (0.5% and 0.7%), dislocation substructures including veins, walls, labyrinth and cells prevailed. This is indicative of dislocation slip mode transition from planar-slip to wavy-slip with increasing strain amplitude.

(3) Dislocation-poor regions (*i.e.*, channels) between dislocation-rich regions (*i.e.*, veins and walls) form as a result of the extensive annihilation of the gliding and cross-slipping screw dislocations. This confirms that wavy-slip contributes to their formation rather than the previously suggested planar-slip in CoCrFeMnNi [11].

(4) Additionally, dislocations in various substructures (*i.e.*, veins, walls and cells) are proven to have different Burgers vectors. This indicates that, apart from the wavy-slip, multiple-slip also contributes to their formation. To further unravel the role of multiple-slip, modeling efforts (*e.g.*, discrete dislocation dynamics) could be beneficial.

22

(5) Increasing cycle number results in dislocation structure evolution from initial tangles and planar slip bands to ill-defined wavy-substructures; and then, finally to their well-defined versions. This dislocation structure evolution is linked to the observed cyclic stress response, *i.e.*, initial cyclic hardening followed by softening and near-steady state until failure.

(6) Distinct dislocation substructure formation in polycrystalline CoCrFeMnNi is dictated more by the constraints from neighboring grains rather than grain orientation. Additionally, the formation of various dislocation structures in a single grain is also linked to the constraint effects from the neighboring grains.

(7) Based on the lower inelastic strain at each cycle, CoCrFeMnNi is expected to show a longer lifetime than the 316L steel at similar strain amplitudes. This suggests that CoCrFeMnNi HEA or its subsets with higher strength (stemming from higher solid solution strengthening) and sufficient ductility could provide enhanced LCF resistance, as compared to conventional FCC steels with similar SFE.

Supplementary material
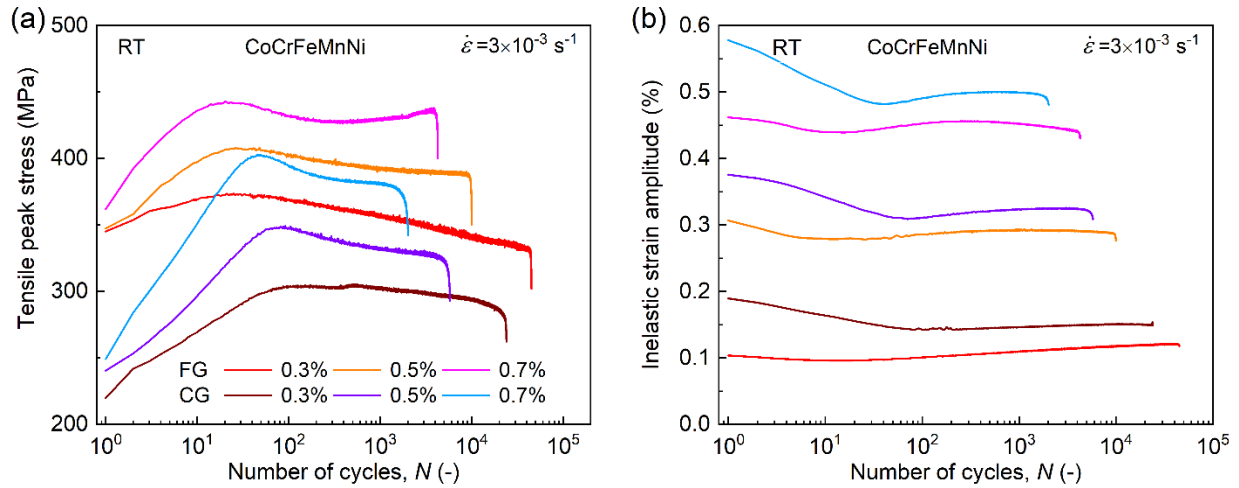
Fig. S1. (a) Tensile peak stress, and (b) inelastic strain amplitude *versus* number of cycles (*N*) curves for fine-grained (FG) [10] and coarse-grained (CG) CoCrFeMnNi under different strain amplitudes at RT. The color legend in (a) is also valid for (b).
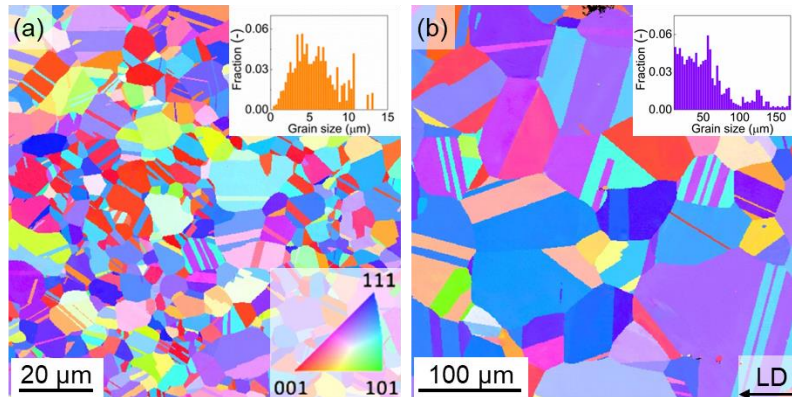
Fig. S2. Representative inverse pole figure (IPF) maps along the swaging direction for (a) fine-grained (FG) [10] and (b) coarse-grained (CG) CoCrFeMnNi, respectively, tested at 0.5% strain amplitude at RT. The grain size distributions of each states were provided in the inset of (a, b). Post-fatigued EBSD investigations for both materials show no significant change in texture, average grain sizes and twins fractions in comparison with the annealed states.

Table S1. Values of **g·b** for perfect dislocations in FCC crystals to identify dislocations Burgers vector **b**.

Plane of dislocations	**g** / **b**	$1\bar{1}1$	$11\bar{1}$	$\bar{2}00$
$(1\bar{1}1)$ or $(1\bar{1}\bar{1})$	½[110]	**0**	1	$\bar{1}$
$(1\bar{1}\bar{1})$ or $(11\bar{1})$	½[101]	1	**0**	$\bar{1}$
$(1\bar{1}1)$ or $(11\bar{1})$	½[011]	**0**	**0**	**0**
(111) or $(11\bar{1})$	½[1$\bar{1}$0]	1	**0**	$\bar{1}$
(111) or $(1\bar{1}1)$	½[10$\bar{1}$]	**0**	1	$\bar{1}$
(111) or $(\bar{1}11)$	½[0$\bar{1}$1]	1	$\bar{1}$	**0**

References

[1] E.P. George, D. Raabe, R.O. Ritchie, High-entropy alloys, Nature Reviews Materials (2019).

[2] E.P. George, W.A. Curtin, C.C. Tasan, High entropy alloys: A focused review of mechanical properties and deformation mechanisms, Acta Materialia (2019).

[3] B. Cantor, I.T.H. Chang, P. Knight, A.J.B. Vincent, Microstructural development in equiatomic multicomponent alloys, Materials Science and Engineering: A 375-377 (2004) 213-218.

[4] K.V.S. Thurston, B. Gludovatz, A. Hohenwarter, G. Laplanche, E.P. George, R.O. Ritchie, Effect of temperature on the fatigue-crack growth behavior of the high-entropy alloy CrMnFeCoNi, Intermetallics 88 (2017) 65-72.

[5] Y.-K. Kim, G.-S. Ham, H.S. Kim, K.-A. Lee, High-cycle fatigue and tensile deformation behaviors of coarse-grained equiatomic CoCrFeMnNi high entropy alloy and unexpected hardening behavior during cyclic loading, Intermetallics 111 (2019) 106486.

[6] Y.Z. Tian, S.J. Sun, H.R. Lin, Z.F. Zhang, Fatigue behavior of CoCrFeMnNi high-entropy alloy under fully reversed cyclic deformation, Journal of Materials Science & Technology 35(3) (2019) 334-340.

[7] A.G. Wang, X.H. An, J. Gu, X.G. Wang, L.L. Li, W.L. Li, M. Song, Q.Q. Duan, Z.F. Zhang, X.Z. Liao, Effect of grain size on fatigue cracking at twin boundaries in a CoCrFeMnNi high-entropy alloy, Journal of Materials Science & Technology (2019).

[8] S.A.A. Shams, G. Jang, J.W. Won, J.W. Bae, H. Jin, H.S. Kim, C.S. Lee, Low-cycle fatigue properties of CoCrFeMnNi high-entropy alloy compared with its conventional counterparts, Materials Science and Engineering: A 792 (2020) 139661.

[9] K. Lu, A. Chauhan, D. Litvinov, M. Walter, A.S. Tirunilai, J. Freudenberger, A. Kauffmann, M. Heilmaier, J. Aktaa, High-temperature low cycle fatigue behavior of an equiatomic CoCrFeMnNi high-entropy alloy, Materials Science and Engineering: A 791 (2020) 139781.

[10] K. Lu, A. Chauhan, M. Walter, A.S. Tirunilai, M. Schneider, G. Laplanche, J. Freudenberger, A. Kauffmann, M. Heilmaier, J. Aktaa, Superior low-cycle fatigue properties of CoCrNi compared to CoCrFeMnNi, Scripta Materialia 194 (2021) 113667.

[11] S. Picak, T. Wegener, S.V. Sajadifar, C. Sobrero, J. Richter, H. Kim, T. Niendorf, I. Karaman, On the Low Cycle Fatigue Response of CoCrNiFeMn High Entropy Alloy with Ultra-fine Grain Structure, Acta Materialia (2020) 116540.

[12] M. Gerland, J. Mendez, P. Violan, B. Ait Saadi, Evolution of dislocation structures and cyclic behaviour of a 316L-type austenitic stainless steel cycled in vacuo at room temperature, Materials Science and Engineering: A 118 (1989) 83-95.

[13] T. Mayama, K. Sasaki, M. Kuroda, Quantitative evaluations for strain amplitude dependent organization of dislocation structures due to cyclic plasticity in austenitic stainless steel 316L, Acta Materialia 56(12) (2008) 2735-2743.

[14] J. Nellessen, S. Sandlöbes, D. Raabe, Effects of strain amplitude, cycle number and orientation on low cycle fatigue microstructures in austenitic stainless steel studied by electron channelling contrast imaging, Acta Materialia 87 (2015) 86-99.

[15] P. Li, S.X. Li, Z.G. Wang, Z.F. Zhang, Unified factor controlling the dislocation evolution of fatigued face-centered cubic crystals, Acta Materialia 129 (2017) 98-111.

[16] D.J. Morrison, Influence of grain size and texture on the cyclic stress-strain response of nickel, Materials Science and Engineering: A 187(1) (1994) 11-21.

[17] D.J. Morrison, J.C. Moosbrugger, Effects of grain size on cyclic plasticity and fatigue crack initiation in nickel, International Journal of Fatigue 19(93) (1997) 51-59.

[18] A.S. Tirunilai, J. Sas, K.-P. Weiss, H. Chen, D.V. Szabó, S. Schlabach, S. Haas, D. Geissler, J. Freudenberger, M. Heilmaier, A. Kauffmann, Peculiarities of deformation of CoCrFeMnNi at cryogenic temperatures, Journal of Materials Research 33(19) (2018) 3287-3300.

[19] A. E2714-13, Standard Test Method for Creep-Fatigue Testing, ASTM International, West Conshohocken, PA, (2013) 1-15.

[20] J. Morrow, Cyclic plastic strain energy and fatigue of metals, Internal friction, damping, and cyclic plasticity, ASTM International1965.

[21] S.S. Manson, Behavior of materials under conditions of thermal stress, National Advisory Committee for Aeronautics 1953.

[22] L.F. Coffin Jr, A study of the effects of cyclic thermal stresses on a ductile metal, Transactions of the American Society of Mechanical Engineers, New York 76 (1954) 931-950.

[23] P. Hirsch, A. Howie, R. Nicholson, D. Pashley, M. Whelan, L. Marton, Electron microscopy, PhT 19(10) (1966) 93.

[24] D.B. Williams, C.B. Carter, The transmission electron microscope, Transmission electron microscopy, Springer1996, pp. 3-17.

[25] Brent Fultz, J. Howe, Transmission Electron Microscopy, (2008).

[26] Y. Li, C. Laird, Cyclic response and dislocation structures of AISI 316L stainless steel. Part 2: polycrystals fatigued at intermediate strain amplitude, Materials Science and Engineering: A 186(1) (1994) 87-103.

[27] F. Otto, A. Dlouhý, C. Somsen, H. Bei, G. Eggeler, E.P. George, The influences of temperature and microstructure on the tensile properties of a CoCrFeMnNi high-entropy alloy, Acta Materialia 61(15) (2013) 5743-5755.

[28] V. Gerold, H.P. Karnthaler, On the origin of planar slip in f.c.c. alloys, Acta Metallurgica 37(8) (1989) 2177-2183.

[29] J. Cohen, M. Fine, Some aspects of short-range order, J. Phys. Radium 23(10) (1962) 749-762.

[30] Q.J. Li, H. Sheng, E. Ma, Strengthening in multi-principal element alloys with local-chemical-order roughened dislocation pathways, Nat Commun 10(1) (2019) 3563.

[31] J. Ding, Q. Yu, M. Asta, R.O. Ritchie, Tunable stacking fault energies by tailoring local chemical order in CrCoNi medium-entropy alloys, Proc Natl Acad Sci U S A 115(36) (2018) 8919-8924.

[32] R. Zhang, S. Zhao, J. Ding, Y. Chong, T. Jia, C. Ophus, M. Asta, R.O. Ritchie, A.M. Minor, Short-range order and its impact on the CrCoNi medium-entropy alloy, Nature 581 (7808) (2020) 283-287.

[33] P. Lukáš, M. Klesnil, J. Krejčí, Dislocations and persistent slip bands in copper single crystals fatigued at low stress amplitude, physica status solidi (b) 27(2) (1968) 545-558.

[34] U. Essmann, H. Mughrabi, Annihilation of dislocations during tensile and cyclic deformation and limits of dislocation densities, Philosophical Magazine A 40(6) (1979) 731-756.

[35] H. Mughrabi, Dislocation wall and cell structures and long-range internal stresses in deformed metal crystals, Acta Metallurgica 31(9) (1983) 1367-1379.

[36] T. Tabata, H. Fujita, M.-A. Hiraoka, K. Onishi, Dislocation behaviour and the formation of persistent slip bands in fatigued copper single crystals observed by high-voltage electron microscopy, Philosophical Magazine A 47(6) (1983) 841-857.

[37] K. Obrtlík, T. Kruml, J. Polák, Dislocation structures in 316L stainless steel cycled with plastic strain amplitudes over a wide interval, Materials Science and Engineering: A 187(1) (1994) 1-9.

[38] M.S. Pham, S.R. Holdsworth, K.G.F. Janssens, E. Mazza, Cyclic deformation response of AISI 316L at room temperature: Mechanical behaviour, microstructural evolution, physically-based evolutionary constitutive modelling, International Journal of Plasticity 47 (2013) 143-164.

[39] P. Lukáš, L. Kunz, Role of persistent slip bands in fatigue, Philosophical Magazine 84(3-5) (2004) 317-330.

[40] S.J. Basinski, Z.S. Basinski, A. Howie, Early stages of fatigue in copper single crystals, The Philosophical Magazine: A Journal of Theoretical Experimental and Applied Physics 19(161) (1969) 899-924.

[41] A. Winter, O. Pedersen, K. Rasmussen, Dislocation microstructures in fatigued copper polycrystals, Acta Metallurgica 29(5) (1981) 735-748.

[42] M. Gerland, P. Violan, Secondary cyclic hardening and dislocation structures in type 316 stainless steel at 600°C, Materials Science and Engineering 84 (1986) 23-33.

[43] M.A. Meyers, O. Vöhringer, V.A. Lubarda, The onset of twinning in metals: a constitutive description, Acta Materialia 49(19) (2001) 4025-4039.

[44] G. Laplanche, A. Kostka, O. Horst, G. Eggeler, E.P. George, Microstructure evolution and critical stress for twinning in the CrMnFeCoNi high-entropy alloy, Acta Materialia 118 (2016) 152-163.

[45] D. Kuhlmann-Wilsdorf, C. Laird, Dislocation behavior in fatigue, Materials Science and Engineering 27(2) (1977) 137-156.

[46] D. Kuhlmann-Wilsdorf, Theory of plastic deformation: - properties of low energy dislocation structures, Materials Science and Engineering: A 113 (1989) 1-41.

[47] L. Kubin, M. Sauzay, Persistent slip bands: The bowing and passing model revisited, Acta Materialia 132 (2017) 517-524.

[48] H. Mughrabi, F. Ackermann, K. Herz, Fatigue mechanisms, ASTM STP 675 (1979) 69.

[49] P. Li, S.X. Li, Z.G. Wang, Z.F. Zhang, Formation mechanisms of cyclic saturation dislocation patterns in [001], [011] and [1̄11] copper single crystals, Acta Materialia 58(9) (2010) 3281-3294.

[50] X.W. Li, Y. Zhou, W.W. Guo, G.P. Zhang, Characterization of dislocation structures in copper single crystals using electron channelling contrast technique in SEM, Crystal Research and Technology: Journal of Experimental and Industrial Crystallography 44(3) (2009) 315-321.

[51] S.M. Copley, B.H. Kear, The dependence of the width of a dissociated dislocation on dislocation velocity, Acta Metallurgica 16(2) (1968) 227-231.

[52] C. Buque, J. Bretschneider, A. Schwab, C. Holste, Dislocation structures in cyclically deformed nickel polycrystals, Materials Science and Engineering: A 300(1) (2001) 254-262.

[53] Y. El-Madhoun, A. Mohamed, M. Bassim, Cyclic stress–strain behavior of polycrystalline nickel, Materials Science and Engineering: A 385(1-2) (2004) 140-147.

[54] N.L. Okamoto, S. Fujimoto, Y. Kambara, M. Kawamura, Z.M. Chen, H. Matsunoshita, K. Tanaka, H. Inui, E.P. George, Size effect, critical resolved shear stress, stacking fault energy, and solid solution strengthening in the CrMnFeCoNi high-entropy alloy, Scientific Reports 6 (2016) 35863.

[55] T. Magnin, C. Ramade, J. Lepinoux, L.P. Kubin, Low-cycle fatigue damage mechanisms of F.c.c. and B.c.c. polycrystals: Homologous behaviour?, Materials Science and Engineering: A 118 (1989) 41-51.

[56] P. Li, S. Li, Z. Wang, Z. Zhang, Fundamental factors on formation mechanism of dislocation arrangements in cyclically deformed fcc single crystals, Progress in Materials Science 56(3) (2011) 328-377.

[57] M.S. Pham, S.R. Holdsworth, Role of microstructural condition on fatigue damage development of AISI 316L at 20 and 300°C, International Journal of Fatigue 51 (2013) 36-48.